



A sea-change: Manganese doped nickel/nickel oxide electrocatalysts for hydrogen generation from seawater

Journal:	<i>Energy & Environmental Science</i>
Manuscript ID	EE-ART-04-2018-000976.R1
Article Type:	Paper
Date Submitted by the Author:	09-May-2018
Complete List of Authors:	<p>Lu, Xunyu; University of New South Wales - Randwick Campus, Particle and Catalysis Research Group, School of Chemical Sciences and Engineering</p> <p>Pan, Jian; University of New South Wales - Randwick Campus, Particle and Catalysis Research Group, School of Chemical Sciences and Engineering</p> <p>Lovell, Emma; University of New South Wales - Randwick Campus, Particle and Catalysis Research Group, School of Chemical Sciences and Engineering</p> <p>Tan, Tze Hao; University of New South Wales - Randwick Campus, Particle and Catalysis Research Group, School of Chemical Sciences and Engineering</p> <p>Ng, Yun Hau; The University of New South Wales, Particle and Catalysis Research Group, School of Chemical Sciences and Engineering</p> <p>Amal, Rose; University of New South Wales - Randwick Campus, Particle and Catalysis Research Group, School of Chemical Sciences and Engineering</p>

A sea-change: Manganese doped nickel/nickel oxide electrocatalysts for hydrogen generation from seawater

Xunyu Lu,* Jian Pan, Emma Lovell, Tze Hao Tan, Yun Hau Ng and Rose Amal*

Particles and Catalysis Research Group, School of Chemical Engineering, The

University of New South Wales, Sydney, NSW 2052, Australia

Email: r.amal@unsw.edu.au

xunyu.lu@unsw.edu.au

Abstract

The practical implementation of electrolytic water splitting systems (especially those powered by renewable energy resources, such as solar and wind) requires active and stable catalysts for the hydrogen evolution reaction (HER). The development of catalysts that can compete with, or exceed, the performance of the exorbitant platinum (Pt)-based benchmark is highly desirable. Here, we demonstrate the development of a highly active HER catalyst electrode, exhibiting Pt-like performances in both neutral electrolytes and natural seawater. The catalyst was obtained by pyrolysing a manganese-based metal organic framework (Mn-MOF) on nickel foam (Ni-F). We discovered for the first time that nickel foam not only acts as the substrate for catalyst growth but also provides nickel species that interact with the Mn-MOF, resulting in the formation of Mn doped nickel oxide/nickel hetero-structures on Ni-F (Mn-NiO-Ni/Ni-F). The potential utilization of this catalyst electrode for commercial applications was demonstrated in a self-customized water electrolyzer pack powered by photovoltaic cells.

Broader Context

The use of photovoltaic-powered electrolytic water splitting systems has the capability of storing the intermittent and diffusive solar energy in the form of hydrogen (H_2). H_2 is a clean and high energy density energy carrier that can be stored and easily distributed. However, the large-scale deployment of such systems requires the development of efficient and cost-effective catalysts for the hydrogen evolution reaction (HER). Ideally, a catalyst that can match, or even exceed, the performance of the expensive platinum (Pt) based benchmark, is necessary for large scale implementation. Further, the generation of H_2 from neutral (or near neutral electrolytes), and even seawater, as opposed to highly alkaline and/or acidic solutions is ideal from a practical implementation perspective. However, to date this has posed a challenge in material development due to the relatively sluggish reaction kinetics in neutral electrolytes. In this work, novel manganese doped nickel oxide/nickel heterostructured arrays were prepared on the skeleton of nickel foam. This facile and scalable synthesis resulted in the formation of manganese-doped nickel/nickel oxide heterostructures with distinct Ni and NiO boundaries. These novel heterostructures achieved high activity, even outperforming the Pt benchmark, in neutral electrolytes and was able generate hydrogen from natural sea water in a self-customized electrolyser pack.

Introduction

The past few decades have witnessed a rapid development in photovoltaic (PV) cells with drastically increased conversion efficiency and significantly lowered fabrication costs. This progress makes PV cells undoubtedly the most promising route at present to harness solar energy.^{1,2} From this, the storage of superfluous electricity generated by PV cells is of crucial importance in order to provide continuous electricity supply, thus overcoming the inherent intermittency of utilizing solar energy.³ A promising strategy to resolve this is the use of electrolytic water splitting systems powered by PV-cells. Ultimately, this means that solar energy can be exploited to produce hydrogen⁴⁻⁶, which can be stored and utilized in H₂ fuel cell stacks to power H₂ vehicles along with households as per demand.⁷ Such a system seems highly feasible, in theory, as both PV cells and hydrogen generators are commercially available. However, in reality, large-scale implementation will not be practical unless the high cost of hydrogen generators can be resolved.

Typically, in hydrogen generators available on the market, the crucial aspect is the catalysts for the electrolyzer pack. Traditional catalysts are normally hindered due to their exorbitant costs for Ir/C, RuO₂ and Pt/C, or the unsatisfying activity for the more economically viable stainless steel and nickel meshes. Therefore, the development of a novel material which has both low cost whilst facilitating high activity is of great interest. Recently, there has been a breakthrough in the development of oxygen evolution reaction (OER) catalysts based on Ni and Fe, which have been reported to exhibit superior catalytic activity to the Ir/C and RuO₂ benchmarks.⁸⁻¹² As a result, a cost-effective hydrogen evolution reaction (HER) catalyst which can exhibit similar or even superior catalytic activity to the Pt/C benchmark may enable the mass-production of cheap and active hydrogen generators in the near future.

For HER catalysts in a commercial hydrogen generator, the following criteria need to be met. The catalyst should (i) facilitate similar, or higher, catalytic activity compared to the Pt/C benchmark, which is essential to minimize the energy loss during electricity to hydrogen conversion; (ii) be comprised of earth-abundant elements, whilst being obtained using cost-effective, facile and scalable preparation methods; (iii) attach firmly to current collectors (including nickel foam, carbon fiber paper and carbon cloth) without using binders whilst being implemented as the HER electrode as a whole in order to reduce the contact resistance as well as avoid catalyst peeling off under vigorous reaction conditions; (iv) be robust, both physically and electrochemically, allowing them to be used for HER for a prolonged duration (> 3,000 h) without physical damage or activity decay. Recently, a tremendous research effort has been focused toward the development of non-precious material-based catalysts for HER. Numerous materials, ranging from transitional metals, metal alloys, nitrides, carbides, oxides to metal-free carbon nanomaterials, have been prepared,¹³⁻¹⁸ and many strategies, including metal/carbon combination,¹⁹⁻²¹ defect engineering,²²⁻²⁴ electronic structure modification²⁵⁻²⁷ and downsizing to atomic scale,²⁸⁻³⁰ have been exploited to further improve catalytic performance. Unfortunately, to date, the fulfillment of the aforementioned requirements for HER catalysts still remains a challenge and thus the search is ongoing.

Herein, we report a novel and cost-effective HER electrode prepared via a simple and scalable synthesis route. The HER electrode consists of a well-ordered manganese doped nickel oxide/nickel hetero-structured arrays on the skeleton of nickel foam (Mn-NiO-Ni/Ni-F). The obtained Mn-NiO-Ni/Ni-F can be utilized directly for HER without further treatment, and is highly active towards HER in neutral electrolytes and natural seawater, showing negligible onset overpotential and

remarkable long-term stability (> 500 h in neutral electrolytes), outperforming the Pt/C benchmark. A customized electrolyzer pack, employing the Mn-NiO-Ni/Ni-F as the cathode along with a previously reported nickel-iron hydroxide on Ni-F (NiFe/Ni-F)¹¹ as the anode, was then assembled. The performance of this customized cell was evaluated, with a high current of 0.2 A (corresponding to a current density of 66.7 mA cm⁻²) obtained at an applied cell voltage of 1.8 V.

Results

Synthesis and characterization. To prepare the HER electrode, a Mn-based metal-organic framework (MOF) was firstly anchored onto the skeleton of a nickel foam (MOF/Ni-F) through hydrothermal treatment. X-ray diffraction (XRD) of the synthesized powder (scratched off from the MOF/Ni-F) exhibits multiple peaks in the small angle range (10-20 °), indicating the successful obtainment of a MOF structure (Figure S1). The MOF/Ni-F was then subjected to a slowly ramped (1 °C min⁻¹) pyrolysis process in an Ar environment to produce the final electrode (refer to Methods for details). Figure S2 shows the photos of pure Ni-F, MOF/Ni-F and the final electrode with distinct colors. The green color of the MOF/Ni-F can be attributed to the deposition of Mn-based MOF layers on the Ni-F skeleton, whilst the black color of the final electrode indicates the carbonization of the MOF resulting in the formation of metal/carbon composites on the Ni-F. Figure 1 a-c displays the scanning electron microscopy (SEM) images of the final electrode at different magnifications. The surface of the skeleton in the obtained electrode exhibits dense, uniform deposits over the entirety of the internal area. This is in contrast to the smooth surface of pure Ni-F (shown in Figure S3). The deposits were tightly packed, forming arrays that resemble the structure of underbrush (Figure 1b). As evident in Figure 1c, under high magnification SEM, the deposits exhibit a nanoflake structure up to several

micrometers wide with very thin thickness. Figure 1d shows the scanning transmission electron microscopy (STEM) image of the deposits scratched off from the electrode. It can be clearly seen through the STEM and the corresponding high angle annular dark field (HAADF-STEM) image that the nanoflake is comprised of carbon matrix (dark area in Figure 1e) with metal nanoparticles (bright spots in Figure 1e) embedded inside, reflecting a typical metal/carbon composite derived from MOF precursors.³¹⁻³³ The energy-dispersive X-ray (EDX) spectroscopy analysis of Figure 1d is shown in Figure S4. As expected, the Mn, C and O are uniformly distributed along the nanoflake structure, which is derived from the Mn-MOF. Surprisingly, a significant amount of Ni nanoparticles are also evident in the composite, exhibiting a dense and uniform distribution (Figure S4b). The only metallic content of the MOF is Mn, and thus, theoretically, Mn should be the sole metal component in the composite derived from it. However, in this study, Ni-F was employed as the substrate for the deposition of Mn-MOF. It is therefore plausible that the Ni-F acts as a source of Ni, which may migrate from the skeleton of the foam to the nearby MOF during the pyrolysis process, eventually resulting in the formation of Ni nanoparticles concomitantly with Mn nanoparticles. To confirm this, composite powders derived from Mn-MOF prepared in the absence of Ni-F were analyzed. Figure S5 represents the STEM measurements and the corresponding elemental mappings of the MnC powder. From Figure S5 it is evident that Mn is the only detectable metallic component in the composite while Ni is absent, thus supporting that Ni-F is the source of Ni species found in the composite. Moreover, if pure Ni-F was subjected to the same pyrolysis process in the absence of Mn-MOF, some nickel nano-islands emerged on the surface (Figure S6), while this morphology is clearly distinctive from

that obtained in the presence of Mn-MOF. The collective results confirm both Mn-MOF and Ni-F are crucial in obtaining the novel Mn/Ni binary metal nanostructures.

As the co-existence of Mn and Ni species in the composite has been confirmed, their corresponding chemical and physical properties need to be evaluated. Figure 1f displays the high magnification STEM image of the area indicated in Figure 1d. Two distinctive nanoparticles can be observed in this image. This was confirmed by the HAADF-STEM analysis, as the metallic component exhibited a high contrast while the possible metal oxide displayed a low contrast (Figure S7). EDX mappings revealed the metal oxide belongs to Mn meanwhile the metallic component associates with Ni (Figure 1g and 1h). The mapping showed that a significant overlapping of Mn species with the Ni nanoparticles (Figure 1g), suggesting the presence of Mn doped Ni nanoparticles. This doping may be ascribed to the migration of Mn atoms during heating treatments.³⁴ Figure 1i represents the O element mapping of the composite. Interestingly, the O is observed uniformly and densely distributed on both the Mn oxide and “metallic” Ni. This phenomenon indicates the Ni species obtained may exist as metal/metal oxide hetero-structures.

To further confirm this assumption, STEM of an individual Ni nanoparticle was studied. The existence of a core-shell structured Ni nanoparticle is clearly evident (Figure 1j), reflected as a lighter shell and a dark core. This conclusion was supported by HAADF-STEM analysis (Figure S8) as the metallic core exhibited a high contrast while the metal oxide shell displayed a low contrast. Moreover, by enlarging the areas marked in Figure 1j, typical lattice fringes with a d spacing of 0.147 nm (Figure 1k) and 0.179 nm (Figure 1l) are detected, which belong to the (220) facet of fcc nickel oxide and (200) facet of the fcc nickel, respectively.^{35,36} The collective microscopic

measurements indicate Mn oxide and NiO-Ni hetero-structured nanoparticles are formed in the composite obtained on Ni-F.

X-ray diffraction (XRD) was utilized to further examine the composition of the prepared electrode. To eliminate interference from the Ni-F substrate, powder XRD was performed on the composites carefully scratched off from the electrode.^{37, 38} As expected, Ni, NiO and MnO phases are evident in the XRD (Figure 2a).³⁹⁻⁴¹ This finding was further confirmed by X-ray photoelectron spectroscopy (XPS). As shown in Figure 2b, the electrode is comprised of Mn, Ni, C and O, which correlates well with the results from EDX mappings. Figure 2c represents the high resolution Ni 2p survey spectrum, with the Ni 2p_{3/2} and Ni 2p_{1/2} peaks detected at 854.5 eV and 872.5 eV, respectively, accompanied by two satellite peaks, corresponding to the spin-orbits of NiO.⁴²⁻⁴⁴ As XPS is a surface analysis technique, the probing depth (~ 5 nm) is larger than the NiO shell (~ 2 nm, Figure 1j), thus a small quantity of metallic Ni is detected, reflected by the shoulder ~ 852.7 eV. The high resolution Mn 2p XPS spectrum (Figure 2d) exhibits two peaks located at 653.0 eV and 641.3 eV, which are the characteristic Mn 2p_{1/2} and Mn 2p_{3/2} peaks of MnO, respectively.^{45, 46} Collectively, the XRD and XPS results confirm a MnO-NiO-Ni/Ni-F electrode has been successfully prepared.

Physical and chemical changes of the MnO-NiO-Ni/Ni-F electrode during HER.

The obtained MnO-NiO-Ni/Ni-F electrode was utilized directly as the working electrode for HER in aqueous solutions without further treatment. Figure 3a depicts the 48 h constant potential electrolysis curve obtained with the MnO-NiO-Ni/Ni-F electrode in 1 M phosphate buffer (PB) solution (pH = 7). A fixed overpotential (η) of 170 mV was applied to the MnO-NiO-Ni/Ni-F electrode, and the corresponding current density (j) was recorded so as to reflect the electrochemical stability of the

catalyst material. During the reaction, composite powders were taken out from the electrode at intervals of 5, 10, 24 and 48 hours for STEM measurements to investigate their changes (physical and chemical) as the reaction progressed. As shown in Figure 3a, the chronoamperometric curve remained almost unchanged over the reaction period, showing a j stabilized $\sim 25 \text{ mA cm}^{-2}$ with minor fluctuations ($< 10\%$). Since electrochemical activity is intrinsically associated with the physical and chemical properties of the catalyst, the stable performance of MnO-NiO-Ni/Ni-F electrode in the PB solution may indicate the absence of critical changes within the composite otherwise it will definitely be reflected as trends in the current density (either ascend or descend).

The STEM images and the corresponding EDX mappings of the MnO-NiO-Ni composites taken from the electrode after 5, 10, 24 and 48 hours of HER, respectively, are shown in Figures S9-S12. Interestingly, even though the HER catalytic performance remained stable during the 48 h reaction, drastic chemical changes were observed. Specifically, after 5 h of reaction, a significant decrease in the presence of MnO nanoparticles within the MnO-NiO-Ni composite is clearly evident by STEM and EDX analysis (Fig. S9). This phenomenon is ascribed to the electrochemical dissolution of MnO species during HER upon the application of a negative bias. In contrast, no MnO dissolution was observed by simply dipping the MnO-NiO-Ni/Ni-F electrode in PB solution without applying potentials. As the reaction progressed, the dissolution of the MnO continued with the presence of MnO further declining after 10 h (Figure S10), and completely vanished after 24 h of reaction duration (Figure S11). Interestingly, Mn species are still detectable in the composite material even after 48 h of HER (Figure S12), corresponding to those doped into the NiO-Ni hetero-structures that are not affected by the external

environment. The dissolution of MnO in the composite was again confirmed by evaluating the PB solution after different reaction increments using inductively coupled plasma mass spectroscopy (ICP-MS). The Mn concentration in the electrolyte increased from 0 to 8.5 ppm during the first 20 h of HER, subsequently remaining stable for the remainder of reaction, which correlates well with results from STEM and EDX measurements.

After 48 h of HER, the catalyst materials remained densely and uniformly coated on the skeleton of Ni-F (shown in the SEM, Figure. S13a) thus confirming their strong binding strength, even resistant to the vigorous gas evolving during HER. Under high magnification (Figure S13b and S13c), the composites exhibited a nanoflake structure with evidence of shrinkage around the edges, compared with the fresh sample (Figure. 1c). This may be a result of the dissolution of MnO nanoparticles. The electrode was then immersed into a fresh PB solution for further HER measurements under identical reaction conditions. Figure 3b and 3c presents the high magnification STEM image and the corresponding EDX mappings of the powder sample after 100 h of HER. Despite all MnO nanoparticles being dissolved, the NiO-Ni hetero-structure remained well maintained throughout the reaction timeframe, with an easily distinguishable Ni core and NiO shell, consistent with the pristine composite before reaction (Figure 1j). The doped Mn species remained detectable in the EDX mapping, indicating their presence in all samples, independent of time period. XPS survey scan (Figure. 3d) of the HER electrode provide an indication of the surface species present after 100 h of reaction. As clearly evident after reaction, no notable Mn species are present whilst the emergence of Na and P peaks are evident, owing to the precipitation from PB solution during HER. The Ni 2p XPS spectrum (Fig. 3e) indicates the detection of the NiO shell. Overall, it is clear that the MnO plays a

negligible role in catalyzing HER as, during the electrochemical dissolution process, the HER catalytic activity of the electrode remains largely unaffected (Fig. 3a), clearly reflected by the highly stable current. Therefore, it is reasonable to deduce that the catalytic activity is arising from the Mn doped Ni-NiO composites (Mn-NiO-Ni) which are supported on Ni-F. Hence, even though both MnO-NiO-Ni/Ni-F and its derived Mn-NiO-Ni/Ni-F (see details in Methods) electrodes exhibit similar activity for HER, the following measurements were all carried out with the latter one for simplistic purpose.

Based on the above observations, deductions can be made about the role of Mn-MOF and its derived MnO nanoparticles in affecting the physical, chemical and electrochemical properties of the Mn-NiO-Ni/Ni-F electrode. (i) During pyrolysis, the Mn-MOF was converted to a MnO/C composite, while the carbon matrix obtained also served as the scaffold for the migration of Ni species, resulting in the formation of the binary metal (Mn/Ni) composites supported on carbon. (ii) The MnO derived from Mn-MOF created a suitable oxidative environment for the immigrated Ni species, neither too strong nor too weak, which is essential for the formation of the well-defined NiO-Ni heterostructure. To confirm this, Ni-MOF was also deposited onto Ni-F followed by a pyrolysis treatment according to the previously established method.⁴⁷ Figure S14 shows the STEM images of the Ni/C composite powder scratched off from the Ni-F surface. As expected, no NiO-Ni heterostructures can be observed in this sample since the boundaries between the two phases were absent under HR-STEM inspection (Figure S14b-d). Moreover, even though Mn-NiO-Ni/Ni-F exhibited smaller roughness factor (RF) than Ni/C/Ni-F (281 for Mn-NiO-Ni/Ni-F, Figure S15, and 433 for Ni/C/Ni-F, adopted from our previous publication⁴⁴), it shows significantly higher HER catalytic activity than the Ni/C/Ni-F

electrode, (Figure S16), further confirming the critical role of Mn-MOF in achieving the active, hetero-structured NiO-Ni composite. As a matter of fact, such well-defined NiO-Ni heterostructures showing clearly detectable boundaries between the two phases, have been hardly achieved in previous reports. (iii) Mn elements were doped into the NiO-Ni composite during pyrolysis. The Mn-doping plays a crucial role in enhancing the HER stability of the NiO-Ni heterostructure, without the observation of noticeable changes (including electrochemical and physical) even after hundreds hours of hydrogen evolution in neutral electrolytes. This effect will be further discussed (*vide supra*).

HER catalytic activity of the Mn-NiO-Ni/Ni-F electrode in neutral electrolytes.

For the majority of the recently developed transition metal-based HER catalysts, alkaline and/or acidic electrolytes are normally required to maximize their catalytic activity.⁴⁸ Neutral electrolytes (such as PB solutions) pose several intrinsic benefits compared to acids and bases, including their benign nature, which minimize adverse environmental impacts as well as prolong the lifetime of devices that are involved.⁴⁹⁵⁰ However, the development of efficient catalysts for HER in neutral electrolytes is highly challenging as a result of the relatively sluggish reaction kinetics, which can be attributed to the lack of hydronium ions and relatively low conductivity.⁵¹ As a result, even though the development of active HER catalysts for neutral electrolytes is of vital practical significance, the achievement remains out of reach.

To evaluate if the prepared electrode can fulfill such a challenging task, in this study, HER was mainly carried out in 1 M PB solution (pH = 7). Figure 4 displays the HER performances of the Mn-NiO-Ni/Ni-F electrode in 1 M PB solution. All tests carried out in this study were performed without compensating the *iR* drop so as to mimic the real usage conditions as resistance is almost ubiquitous regardless of the

efforts that have been devoted to reducing it.⁵² The *i*R-corrected curve is shown in the supplementary information (Figure S17) for the interest of readers. Figure 4a exhibits the polarization curves obtained with Mn-NiO-Ni/Ni-F, Pt/C on Ni-F (Pt/C/Ni-F) and bare Ni-F. Both Mn-NiO-Ni/Ni-F and Pt/C/Ni-F are highly active for HER, showing ~ 0 mV of onset overpotentials. Surprisingly, even though Pt/C/Ni-F exhibited slightly higher activity than Mn-NiO-Ni/Ni-F at $\eta < 100$ mV, our catalyst clearly outperformed Pt/C at $\eta \geq 100$ mV, reflected by the larger *j* that was achieved (24 mA cm⁻² with Pt/C/Ni-F and 35 mA cm⁻² with Mn-NiO-Ni/Ni-F at $\eta = 200$ mV). The high activity of the Mn-NiO-Ni/Ni-F electrode can be attributed to the Mn-NiO-Ni composites on its skeleton according to the following reasons, (i) no HER response was obtained with bare Ni-F within overpotential ranged from 0 to 200 mV (Figure 4a), (ii) hydrogen evolution can be clearly observed on a Mn-NiO-Ni composite coated glassy carbon disk electrode as soon as the applied potential reaching 0 V using the rotating ring disc electrode (RRDE) technique (Figure 4b, see details in Methods).

Moreover, to confirm the current mainly originated from hydrogen evolution as opposed to the response of capacitance, a multi-step chronopotentiometric curve was carried out with Mn-NiO-Ni/Ni-F in the low overpotential range. As displayed in Figure 4c, the applied potential decreased from -0.02 V to -0.08 V with a decrement of 10 mV per 1000 seconds, with the corresponding changes of *j* being recorded. At -0.02 V, it took ~ 500 s for the *j* to stabilize at 4.5 mA cm⁻², and remained unchanged at this value for the remaining 500 s. Meanwhile, steady bubble evolution was observed on the surface of electrode during the entire reaction duration. For all the other applied potentials, the *j* stabilized immediately upon the change of bias, with a stable *j* of 10 mA cm⁻² obtained at -0.08 V. This value corresponds well with the *j*

obtained from polarization curves (Figure 4a), indicating the current is mainly corresponding to hydrogen evolution rather than capacitance. All three electrodes displayed relatively large Tafel slopes (Figure 4d, derived from Figure 4a) owing to the un-compensated system impedance. Albeit, Mn-NiO-Ni/Ni-F exhibited the smallest Tafel slope among the electrodes tested, which correlates well with its exceptional HER activity.

As aforementioned, stability is another issue that severely limits HER catalysts in neutral electrolytes. The catalytic activity obtained with Pt/C/Ni-F dropped dramatically after only two cycles of polarization scan (shown in Fig. S18). The j at -0.3 V decreased from $\sim 35 \text{ mA cm}^{-2}$ with the first scan to merely $\sim 20 \text{ mA cm}^{-2}$ for the second scan. It was observed that a significant amount of Pt/C powder peeled off from the Ni-F substrate during HER. The preparation of Pt/C/Ni-F electrode has been repeated and the deterioration was always observed, despite Nafion binders being added in an attempt to strengthen the binding between Pt/C and the skeleton of Ni-F. It should be noted that such physical instability was not observed with the Pt/C/Ni-F electrode when used in alkaline solutions. Fortunately, owing to the unique design and preparation of the Mn-NiO-Ni/Ni-F, the binding strength between the catalyst and the supporting Ni-F was strong enough to sustain the harsh reaction environment. Figure 4e represents the long-term stability test of the electrode in 1 M PB solution. At an applied η of 80 mV, the electrode delivered a relatively high $j \sim 10 \text{ mA cm}^{-2}$, which remained constant during the 55 h reaction period. Moreover, the stability was maintained even after several power interruptions and under relatively high current densities ($\sim 40 \text{ mA cm}^{-2}$, Figure S19), further confirming the robustness of the Mn-NiO-Ni/Ni-F electrode. As a matter of fact, our catalyst has been tested for more than 500 h in the neutral electrolyte, without the observation of any decay in catalytic

activity.

Overall, the novel Mn-NiO-Ni/Ni-F facilitated high activity as well as exceptional stability for HER in neutral electrolytes. The generation of hydrogen with Mn-NiO-Ni/Ni-F during HER was verified by gas chromatography (GC) with a thermal conductive detector (TCD), as shown in Figure 4f. By comparing the concentration of hydrogen and that calculated from the charge consumed during the reaction, a Faradaic efficiency > 95% was obtained by the conclusion of a 2 h reaction session, indicating that the majority of charge consumed during reaction was used for the generation of hydrogen. The HER performance of the Mn-NiO-Ni/Ni-F electrode was also compared with other recently reported high-performing catalysts in neutral electrolytes, as summarized in Table S1. Compared to all the catalyst materials shown in Table S1, Mn-NiO-Ni/Ni-F is among the most active for HER, demonstrating the lowest overpotentials for reaction commencement as well as reaching the j of 10 mA cm^{-2} , albeit without compensating the systematic iR drop. Such evidence further emphasizes the great potential of Mn-NiO-Ni/Ni-F as satisfying candidates for HER in the natural seawater.

HER catalytic activity of the Mn-NiO-Ni/Ni-F electrode in natural seawater.

Seawater is the most abundant water resource on this planet. If electrolytic hydrogen generation could be directly carried out in seawater without further treatment (including purification and desalination), it has potential to be greatly beneficial to many coastal countries and islands where freshwater is scarce. However, electrocatalytic HER in seawater is extremely challenging due to its intrinsic low conductivity (as compared with 1 M KOH) and highly corrosive nature, resulting in activity and stability issues impacting most of the catalyst materials examined.^{53, 54} Therefore, the search for an active and durable HER catalyst that can be used in

natural seawater, rather than buffered or simulated seawater, is of great significance. In this study, the Mn-NiO-Ni/Ni-F electrode was further evaluated in natural seawater. The seawater used throughout this study was obtained from Maroubra Beach (Sydney, Australia) with a measured pH value of ~ 8.2 . Figure 5a represents the polarization curves obtained with the Mn-NiO-Ni/Ni-F, Pt/C/Ni-F and Ni-F electrodes, respectively. Even in seawater, the Mn-NiO-Ni/Ni-F exhibited superior HER activity to the Pt/C/Ni-F, showing lower onset overpotential (50 mV compared with 100 mV of Pt/C/Ni-F). Within the whole potential range tested, Mn-NiO-Ni/Ni-F exhibited higher j than Pt/C/Ni-F. For instance, at -0.17 V, a j of 10 mA cm^{-2} is obtained with Mn-NiO-Ni/Ni-F while the j obtained with Pt/C/Ni-F is 7.5 mA cm^{-2} . Overall, this indicates that Mn-NiO-Ni/Ni-F is highly active in catalyzing HER in seawater, which not only far exceeds the recently reported CoMoP@C,⁵⁵ NiMoS on carbon cloth,⁵⁶ and U-CNT-900⁵⁴ composite materials, but also outperforms the Pt/C benchmark under identical operational conditions. The extraordinary catalytic performance is also attributed to the Mn-NiO-Ni composite on Ni-F, since the bare Ni-F calls for $\sim 300 \text{ mV}$ of η just to initiate HER in seawater (Figure 5a).

Aside from activity, stability is another critical issue limiting the progress of HER and OER catalysis in seawater.^{57, 58} Seawater contains a variety of anions including chloride, sulfate, bicarbonate, bromide and fluorides. During OER, these anions, especially chlorides, have a tendency to limit the process through the chlorine evolution reaction.^{57, 58} On the other hand, the cations in seawater, such as sodium, calcium, and magnesium, may deposit on the surface of electrode under the conditions for HER. This deposition results in blockage of active sites thereby reducing the accessible surface area, eventually resulting in catalyst deactivation.

Consequently, an in-depth study of the stability of the Mn-NiO-Ni/Ni-F electrode during HER in seawater is essential.

Interestingly, Mn-NiO-Ni/Ni-F remains capable of retaining the initial high catalytic activity in seawater even after prolonged usage. As shown in Figure 5b, the Mn-NiO-Ni/Ni-F can deliver a $j \sim 7 \text{ mA cm}^{-2}$, at a fixed η of 140 mV. Whilst minor fluctuations are evident during the entirety of the reaction session, the performance remained almost unchanged by the end of the 14 h reaction. Meanwhile, vigorous and constant bubble evolution was observed on the electrode surface (Video S1), confirming the generation of hydrogen from seawater. However, contradictory results regarding stability are obtained with GC analysis as shown in Figure 5c. The FE of H_2 reached $\sim 100\%$ within in the first hour, and subsequently deviated significantly from linearity, ending with merely 70% by the conclusion of a 7 h reaction session. This deviation indicates the occurrence of side reactions within the system that consumes 30 % of the total charge. Figure 5d shows additional two chronoamperometric measurements with the Mn-NiO-Ni/Ni-F electrode at the fixed η of 140 mV with a 24 h interval between the three measurements. Despite all curves are stabilizing during their individual reaction period, the j decreased steadily from the initial 7 mA cm^{-2} to 5 and 3 mA cm^{-2} for the second and third measurements, respectively. Additionally, a white deposit was evident on the Mn-NiO-Ni/Ni-F electrode after the initial 14 h of reaction (Figure S20). The above observations indicate the occurrence of electrodeposition during HER in seawater on the electrode. This ultimately consumed a significant portion of total charge and resulted in the blockage of active sites whilst degrading catalytic performance. XPS analysis further confirms the precipitates are mainly comprised of Na, Ca and Mg salts; the typical components of natural seawater (green line in Figure 5e). To regain the activity of the Mn-NiO-

Ni/Ni-F electrode being used in seawater, the electrode was immersed in dilute acid (0.05 M HCl) for 20 min under static conditions. This treatment was capable of removing the salts deposited (Figure S20c), without dissolving the Mn-NiO-Ni composite. XPS analysis (red line in Figure 5e) further showed that only a trace amount of Mg was remained on the electrode (~ 0.5 at%) after acid washing. It is interesting to note that regardless of the reaction environment (PB solution, seawater or acidic treatment), the Ni 2p XPS spectra obtained with the electrodes are always close to identity (Figure S21 and Figure 3e). This observation indicates the robustness of the NiO-Ni heterostructure in the Mn-NiO-Ni composite, which can sustain the harsh reaction environment. The acid-treated electrode was subsequently reused for a chronoamperometric experiment in seawater at the same η of 140 mV (Figure 5f). The j after 5 h of electrolysis stabilized ~ 7 mA cm⁻². This performance was almost identical to the fresh Mn-NiO-Ni/Ni-F electrode (Figure 5d), indicating the efficacy of the acid treatment in cleaning the electrode. Thus, it can be concluded that a mild acid treatment can regain the activity of Mn-NiO-Ni/Ni-F electrodes after being used in seawater over the long-term.

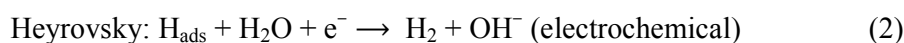
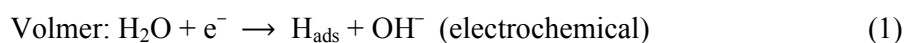
Discussion

The exceptional HER catalytic activity of the Mn-NiO-Ni/Ni-F electrode can be ascribed to the following factors.

(i) The adoption of Ni-F as the substrate. During the past few years, Ni-F has been extensively exploited as the building block for freestanding electrodes that can be used directly in energy conversion reactions. The benefit of using Ni-F is mainly attributed to its unique structural properties, which enables the deposition of large amount of catalyst materials as well as the formation of hierarchical porosities.^{11, 59, 60} Such physical advantages assist in the achievement of the 3D, freestanding Mn-NiO-

Ni/Ni-F electrode, which undeniably contributes to the outstanding HER catalytic activity obtained. Apart from the physical features, in this study, Ni-F was employed as the source of Ni species for the first time, which can provide Ni element that migrate to and interact with the deposited Mn-MOF, resulting in the eventual formation of the Mn/Ni binary composite upon pyrolysis.

(ii) The formation of well-defined NiO-Ni heterostructures. It has been well established that in near neutral (pH \sim 7) electrolytes, HER proceeds via the following steps:^{61, 62}



The reaction will happen through either a Volmer-Tafel pathway or a Volmer-Heyrovsky pathway depending on the applied overpotential.⁶³⁻⁶⁵ In both pathways, the Volmer process is involved where the adsorbed water molecule is electrochemically reduced to H atoms and OH⁻ ions. The Volmer step, especially in alkaline and neutral solutions, requires a significant amount of activation energy (E_a),⁶⁵ thereby resulting in relatively sluggish HER reaction kinetics comparing to that carried out in acidic media. The large E_a associated with the Volmer step can be diminished via weakening the H-OH bond in water molecules. This can be achieved via tailor-making the surface sites to present adjacent metal/metal oxide phases, according to several previous reports.^{25, 26, 66} Specifically, the metal oxide sites tend to attract OH⁻ ions via the electrostatic interactions meanwhile the nearby metallic sites has an affinity for H-bonding, thereby weakening the H-OH bond in water. In this study, a well-defined NiO-Ni heterostructure has been successfully obtained that exhibited clear boundaries between the two phases (Figure 1j and 3b). Therefore, it is plausible to deduce that

during HER, the NiO phase and Ni phase worked synergistically to weaken the water molecules, resulted in lowered E_a and significantly enhanced HER activity. Furthermore, the presence of numerous voids can be observed within the NiO shell under a high resolution HAADF-STEM image (Figure S22), which is also beneficial for HER as a greater amount of adjacent NiO and Ni phases are accessible for HER to take place.

(iii) Doping the NiO-Ni with Mn. Doping Mn element into the NiO-Ni heterostructure brings several benefits for the resultant composite. First of all, the Mn-doping resulted in improved catalytic activity of the NiO-Ni composite in HER. Similar to the effects reported previously, the presence of an alien metal component (in this case Mn) may reduce the free energy of hydrogen adsorption on catalyst surfaces thereby facilitating the occurrence of HER^{67,68}. To further confirm this, a pristine NiO-Ni heterostructured composite, without Mn doping, was prepared via thermal oxidation, and loaded on the Ni-F (NiO-Ni/Ni-F) for comparison (preparation details can be found in the Supporting Information with the composite shown in Figure S23). When used in seawater, Mn-NiO-Ni/Ni-F exhibited far better HER catalytic activity than the NiO-Ni/Ni-F, showing lower onset overpotential and higher current densities at any given potential (Figure S24), confirming the positive role Mn-doping played in catalyzing HER. To further prove the enhancement effects from Mn-doping, we carried out the electrochemical impedance spectroscopy (EIS) measurements of both Mn-NiO-Ni/Ni-F and NiO-Ni/Ni-F electrodes in 1 M KOH at an applied overpotential of 50 mV. As shown in Figure S25, the Mn-NiO-Ni/Ni-F exhibited much smaller EIS semicircular diameter than the NiO-Ni/Ni-F, indicating Mn-NiO-Ni/Ni-F has smaller impedance (including contact and transfer), and faster reaction kinetics for HER than the NiO-Ni/Ni-F.⁶⁹

Besides that, the presence of Mn inside NiO-Ni will prolong the stability of the Mn-NiO-Ni/Ni-F in HER. In a previous report, Gong et.al found the activity of NiO-Ni heterostructure deteriorated after merely 24 h of HER operation, and the heterostructures were oxidized into large NiO aggregates owing to the possible attack of dissolved oxygen species or oxygen gas migrated from the counter electrode.⁷⁰ As a distinctive comparison, the HER activity of Mn-NiO-Ni/Ni-F was barely changed for a reaction duration of several hundreds of hours, accompanied by clearly detectable core-shell structure even after 100 h of usage (Figure 3b). Figure 6a shows the cyclic voltammetric (CV) curves obtained with the Mn-NiO-Ni/Ni-F electrodes after 20 and 50 hours of HER in 1 M PB solution at a constant overpotential of 170 mV. The oxidation peaks observed in the CV curves can be ascribed to the Ni²⁺/Ni^{δ+} ($\delta \geq 3$) transformation.⁷⁰ It is interesting to observe the peak areas of Ni²⁺/Ni^{δ+} for these two electrodes are almost identical, indicating the prolonged usage of the Mn-NiO-Ni/Ni-F electrode in HER will not induce the generation of more Ni²⁺ species within the Mn-NiO-Ni composite, which correlates well with the results obtained by HR-STEM (Figure 3b and 3c). Moreover, the HER polarization curve obtained with the Mn-NiO-Ni/Ni-F before and after 100 h of HER in 1 M PB solution are almost identical, showing similar onset potentials and close to identity current densities at any given potentials (Figure 6b), further confirming the presence of Mn has effectively prevent the NiO-Ni heterostructure from being oxidized during HER. The enhanced stability may be ascribed to the possible formation of Mn blended NiO composites (e.g. NiMnOx) on the surface of NiO-Ni that helps to improve oxygen resistivity, similar to the effects reported in the case of Cr₂O₃ blended with NiO⁷⁰ and the enhanced HER catalytic activity of the Mn-NiO-Ni/Ni-F electrode (fast hydrogen bubbles

formation and dissipation) that minimizes the contact of the NiO outer-layer with oxygen species in the solution.

Due to the promising performance exhibited by the Mn-NiO-Ni/Ni-F electrode, we further extended its application as the cathode in a customized water electrolyzer cell (Figure S26) whereby a previously reported nickel-iron hydroxide supported on nickel foam (NiFe/Ni-F)¹¹ was employed as the anode (details can be referred to Figure S26-Figure S28). The customized cell was highly active in splitting water, and only calls for 200 mV and 320 mV of overpotential to initiate the reaction as well as reach the j of 10 mA cm⁻², respectively (Figure S29a). Moreover, at a cell voltage of 1.8 V, a relatively high current of 0.2 A ($j > 66$ mA cm⁻²) was achieved, with vigorous bubble evolution visualized within the cell (Figure S29b and Video S2).

In summary, we have successfully synthesized a Mn doped NiO/Ni heterostructured electrode by pyrolyzing a Mn-MOF/Ni-F precursor in an inert environment. The prepared material was highly active for HER in both neutral electrolytes and natural seawater, exhibiting a Pt-like catalytic activity. Moreover, when used in natural seawater, the obtained electrode achieved catalytic performances that are even superior to the Pt/C benchmark, exhibiting lower onset overpotential, higher current density at any given potentials as well as exceptional durability. A customized water electrolyzer cell was built employing the Mn-NiO-Ni/Ni-F electrode as the cathode, which can be readily integrated with commercially available solar panels, enabling a direct conversion of solar energy to hydrogen fuel upon the illumination of sunlight (Figure S30 and Video S3).

Methods

Preparation of Mn-MOF/Ni-F and Mn-MOF. Nickel foam (Ni-F, Goodfellow) was sonicated in 5 M HCl for 20 min to remove the native oxide layer on the surface and

left dry in air. The two ends of Ni-F pieces were carefully wrapped by Teflon tape, then placed in a 100 mL Teflon-line autoclave. 70 mg of $\text{Mn}(\text{NO}_3)_2 \cdot 4\text{H}_2\text{O}$ and 67.2 mg of 4,4'-biphenyldicarboxylic acid were dissolved in 40 mL of water and 40 mL of dimethylformamide (DMF), respectively, and allowed to stir for 0.5 h before combining in the autoclave with Ni-F. The mixture was subjected to a hydrothermal reaction at 110 °C for 48 h, and allowed to cool down naturally. The Ni-F was then collected and rinsed thoroughly with water to afford Mn-MOF/Ni-F. Mn-MOF was prepared according to the same experimental procedures except the presence of Ni-F in the autoclave.

Preparation of MnO-NiO-Ni/Ni-F, MnO/C and pyrolysed Ni-F

The MnO-NiO-Ni/Ni-F, MnO/C and pyrolysed Ni-F were prepared via calcining the Mn-MOF/Ni-F, Mn-MOF and pure Ni-F at 700 °C for 3 h in a tube furnace under an Ar environment. The ramping rate is 1 °C min⁻¹. The subsequent Mn-NiO-Ni/Ni-F electrode was obtained by performing the chronoamperometric measurement with the MnO-NiO-Ni/Ni-F working electrode in 1 M PB solution with a constant applied overpotential of 170 mV for at least 20 h. The amount of Mn-NiO-Ni on Ni-F is calculated $\sim 0.25 \text{ mg cm}^{-2}$.

Physical and Chemical Characterization

XPS was performed on a Thermo ESCALAB250i X-ray Photoelectron Spectrometer. SEM was carried out using a JEOL 7001F with a 15 kV accelerating voltage. TEM was performed using a Philips CM 200 microscope. XRD was performed on a PANalytical X'Pert instrument. STEM was performed using a JEOL JEM-ARM200F microscope. ICP-MS characterizations were carried out on a PerkinElmer Quadrupole Nexion ICPMS.

Electrochemical Characterization

All electrochemical measurements were carried out with a CHI 750E electrochemical workstation (CH Instrument, Texas). Mn-NiO-Ni/Ni-F was directly employed as the working electrode without additional treatments. For the Pt/C benchmark (20 wt% of Pt, Sigma-Aldrich), 5mg of the powder sample was dispersed in 1mL water and ethanol mixture (1:1 volume ratio), followed by the addition of 25 μL of Nafion 117 solution (Sigma-Aldrich) as the binder. The mixture was sonicated thoroughly to form homogeneous ink, which was subsequently drop-casted on a Ni-F substrate (Pt/C/Ni-F) with the catalyst loading of 0.5 mg cm^{-2} , and used as the working electrode for the following HER activity measurements. The HER polarization curves were obtained in a traditional three-electrode system, employing Mn-NiO-Ni/Ni-F, Pt/C/Ni-F and pure Ni-F as the working electrodes, graphite rod as the counter electrode and saturated calomel electrode (SCE) as the reference electrode. Three types of electrolytes, namely 1 M phosphate buffer solution (PB, pH = 7), natural seawater (pH \sim 8.2) and 1 M KOH (pH = 14) were used for the HER activity measurements. Rotating ring disc electrode (RRDE) measurements were carried out with a Pt ring glassy carbon disc electrode (ALS Co. Ltd). Specifically, Mn-NiO-Ni composites were carefully scratched off from the Mn-NiO-Ni/Ni-F electrode and prepared into catalyst ink (details refer to the preparation of Pt/C ink), and 3 μL of the catalysts ink was drop-casted onto the surface of the glassy carbon disk, and allowed to dry in air. The potential of the Pt ring was set at 0.33 V vs. RHE to detect the hydrogen produced on the disc via the hydrogen oxidation reaction (HOR). All measured potentials were calibrated to RHE using the following equation: $E_{\text{RHE}} (\text{V}) = E_{\text{SCE}} (\text{V}) + 0.245 + 0.059 \times \text{pH}$. In this study, all electrochemical measurements were performed without correcting the iR drop. Chronoamperometric measurements were obtained under the

same experimental setup, expect a glass frit separated Pt wire was employed as the counter electrode. The current density mentioned in this study was based on geometric surface area.

Conflicts of interest

There are no conflicts to declare

Acknowledgements

All material and surface characterizations were carried out at Mark Wainwright Analytical Centre (MWAC), UNSW. We thank Dr. Bin Gong from MWAC for the XPS measurements. We also thank Dr David Mitchell from University of Wollongong Electron Microscopy Centre for his assistance in HAADF-STEM measurements. The work was supported by the Australian Research Council (ARC) under the Laureate Fellowship Scheme FL-140100081 and Discovery Early Career Researcher Award DE170100375.

References

1. M. A. Green and S. P. Bremner, *Nat Mater*, 2017, **16**, 23-34.
2. M. A. Green, *Nat Energy*, 2016, **1**.
3. N. S. Lewis and D. G. Nocera, *P Natl Acad Sci USA*, 2006, **103**, 15729-15735.
4. J. Y. Jia, L. C. Seitz, J. D. Benck, Y. J. Huo, Y. S. Chen, J. W. D. Ng, T. Bilir, J. S. Harris and T. F. Jaramillo, *Nat Commun*, 2016, **7**.
5. A. Nakamura, Y. Ota, K. Koike, Y. Hidaka, K. Nishioka, M. Sugiyama and K. Fujii, *Appl Phys Express*, 2015, **8**.
6. J. S. Luo, J. H. Im, M. T. Mayer, M. Schreier, M. K. Nazeeruddin, N. G. Park, S. D. Tilley, H. J. Fan and M. Gratzel, *Science*, 2014, **345**, 1593-1596.
7. S. Giddey, S. P. S. Badwal, A. Kulkarni and C. Munnings, *Prog Energy Combust*, 2012, **38**, 360-399.
8. R. D. L. Smith, M. S. Prevot, R. D. Fagan, Z. P. Zhang, P. A. Sedach, M. K. J. Siu, S. Trudel and C. P. Berlinguette, *Science*, 2013, **340**, 60-63.
9. B. Zhang, X. L. Zheng, O. Voznyy, R. Comin, M. Bajdich, M. Garcia-Melchor, L. L. Han, J. X. Xu, M. Liu, L. R. Zheng, F. P. G. de Arquer, C. T. Dinh, F. J. Fan, M. J. Yuan, E. Yassitepe, N. Chen, T. Regier, P. F. Liu, Y. H. Li, P. De Luna, A. Janmohamed, H. L. L. Xin, H. G. Yang, A. Vojvodic and E. H. Sargent, *Science*, 2016, **352**, 333-337.

10. L. Trotochaud, S. L. Young, J. K. Ranney and S. W. Boettcher, *J Am Chem Soc*, 2014, **136**, 6744-6753.
11. X. Y. Lu and C. A. Zhao, *Nat Commun*, 2015, **6**.
12. M. Gong and H. J. Dai, *Nano Res*, 2015, **8**, 23-39.
13. X. X. Zou and Y. Zhang, *Chem Soc Rev*, 2015, **44**, 5148-5180.
14. P. C. K. Vesborg, B. Seger and I. Chorkendorff, *J Phys Chem Lett*, 2015, **6**, 951-957.
15. A. R. Zeradjanin, J. P. Grote, G. Polymeros and K. J. J. Mayrhofer, *Electroanal*, 2016, **28**, 2256-2269.
16. T. Ling, D.-Y. Yan, H. Wang, Y. Jiao, Z. Hu, Y. Zheng, L. Zheng, J. Mao, H. Liu, X.-W. Du, M. Jaroniec and S.-Z. Qiao, *Nature Communication*, 2017, **8**.
17. Y. Zheng, Y. Jiao, A. Vasileff and S.-Z. Qiao, 2017, DOI: <https://doi.org/10.1002/anie.201710556>
18. J. Liu, D. Zhu, T. Ling, A. Vasileff and S.-Z. Qiao, *Nano Energy*, 2017, **40**, 264-273.
19. J. Deng, P. J. Ren, D. H. Deng and X. H. Bao, *Angew Chem Int Edit*, 2015, **54**, 2100-2104.
20. J. S. Li, Y. Wang, C. H. Liu, S. L. Li, Y. G. Wang, L. Z. Dong, Z. H. Dai, Y. F. Li and Y. Q. Lan, *Nat Commun*, 2016, **7**.
21. H. Y. Jin, J. Wang, D. F. Su, Z. Z. Wei, Z. F. Pang and Y. Wang, *J Am Chem Soc*, 2015, **137**, 2688-2694.
22. G. L. Ye, Y. J. Gong, J. H. Lin, B. Li, Y. M. He, S. T. Pantelides, W. Zhou, R. Vajtai and P. M. Ajayan, *Nano Lett*, 2016, **16**, 1097-1103.
23. J. F. Xie, J. J. Zhang, S. Li, F. Grote, X. D. Zhang, H. Zhang, R. X. Wang, Y. Lei, B. C. Pan and Y. Xie, *J Am Chem Soc*, 2014, **136**, 1680-1680.
24. J. F. Xie, H. Zhang, S. Li, R. X. Wang, X. Sun, M. Zhou, J. F. Zhou, X. W. Lou and Y. Xie, *Adv Mater*, 2013, **25**, 5807-+.
25. M. Gong, W. Zhou, M. C. Tsai, J. G. Zhou, M. Y. Guan, M. C. Lin, B. Zhang, Y. F. Hu, D. Y. Wang, J. Yang, S. J. Pennycook, B. J. Hwang and H. J. Dai, *Nat Commun*, 2014, **5**.
26. D. Strmcnik, M. Uchimura, C. Wang, R. Subbaraman, N. Danilovic, D. van der Vliet, A. P. Paulikas, V. R. Stamenkovic and N. M. Markovic, *Nat Chem*, 2013, **5**, 300-306.
27. B. You, X. Liu, G. X. Hu, S. Gul, J. Yano, D. E. Jiang and Y. J. Sun, *J Am Chem Soc*, 2017, **139**, 12283-12290.
28. H. J. Qiu, Y. Ito, W. T. Cong, Y. W. Tan, P. Liu, A. Hirata, T. Fujita, Z. Tang and M. W. Chen, *Angew Chem Int Edit*, 2015, **54**, 14031-14035.
29. W. G. Liu, L. L. Zhang, W. S. Yan, X. Y. Liu, X. F. Yang, S. Miao, W. T. Wang, A. Q. Wang and T. Zhang, *Chem Sci*, 2016, **7**, 5758-5764.
30. H. W. Liang, S. Bruller, R. H. Dong, J. Zhang, X. L. Feng and K. Mullen, *Nat Commun*, 2015, **6**.
31. Y. Y. Lu, Y. T. Wang, H. L. Li, Y. Lin, Z. Y. Jiang, Z. X. Xie, Q. Kuang and L. S. Zheng, *Acs Appl Mater Inter*, 2015, **7**, 13604-13611.
32. T. Y. Ma, S. Dai, M. Jaroniec and S. Z. Qiao, *J Am Chem Soc*, 2014, **136**, 13925-13931.
33. M. Abirami, S. M. Hwang, J. Yang, S. T. Senthilkumar, J. Kim, W. S. Go, B. Senthilkumar, H. K. Song and Y. Kim, *Acs Appl Mater Inter*, 2016, **8**, 32778-32787.
34. W. B. Zhang, Y. Du, L. J. Zhang, H. H. Xu, S. H. Liu and L. Chen, *Calphad*, 2011, **35**, 367-375.

35. S. Z. Khan, Y. Yuan, A. Abdolvand, M. Schmidt, P. Crouse, L. Li, Z. Liu, M. Sharp and K. G. Watkins, *J Nanopart Res*, 2009, **11**, 1421-1427.
36. Z. F. Jiang, J. M. Xie, D. L. Jiang, X. J. Wei and M. Chen, *Crystengcomm*, 2013, **15**, 560-569.
37. N. Feng, D. K. Hu, P. Wang, X. L. Sun, X. W. Li and D. Y. He, *Phys Chem Chem Phys*, 2013, **15**, 9924-9930.
38. B. L. Hu, X. Y. Qin, A. M. Asiri, K. A. Alamry, A. O. Al-Youbi and X. P. Sun, *Electrochim Acta*, 2013, **107**, 339-342.
39. X. Z. Wang, S. Qiu, G. X. Lu, C. Z. He, J. R. Liu, L. Q. Luan and W. Liu, *Crystengcomm*, 2014, **16**, 1802-1809.
40. B. Liu, X. L. Hu, H. H. Xu, W. Luo, Y. M. Sun and Y. H. Huang, *Sci Rep-Uk*, 2014, **4**.
41. J. H. Kim, S. H. Kang, K. Zhu, J. Y. Kim, N. R. Neale and A. J. Frank, *Chem Commun*, 2011, **47**, 5214-5216.
42. W. W. Liu, C. X. Lu, X. L. Wang, K. Liang and B. K. Tay, *J Mater Chem A*, 2015, **3**, 624-633.
43. C. Guan, Y. D. Wang, Y. T. Hu, J. L. Liu, K. H. Ho, W. Zhao, Z. X. Fan, Z. X. Shen, H. Zhang and J. Wang, *J Mater Chem A*, 2015, **3**, 23283-23288.
44. S. Oswald and W. Bruckner, *Surf Interface Anal*, 2004, **36**, 17-22.
45. Y. M. Sun, X. L. Hu, W. Luo and Y. H. Huang, *J Mater Chem*, 2012, **22**, 19190-19195.
46. H. Xia, Y. H. Wan, F. Yan and L. Lu, *Mater Chem Phys*, 2014, **143**, 720-727.
47. X. Lu, X. Tan, D.-W. Wang, Y. H. Ng, H. A. Tahini, H. Tan, W. Yan, S. C. Smith and R. Amal, *Advanced Sustainable Systems*, 2017, **1**, 1700032-n/a.
48. T. Shinagawa and K. Takanaabe, *J Phys Chem C*, 2015, **119**, 20453-20458.
49. X. Y. Lu and C. Zhao, *J Mater Chem A*, 2013, **1**, 12053-12059.
50. Y. J. Sun, C. Liu, D. C. Grauer, J. K. Yano, J. R. Long, P. D. Yang and C. J. Chang, *J Am Chem Soc*, 2013, **135**, 17699-17702.
51. T. Shinagawa and K. Takanaabe, *J Phys Chem C*, 2016, **120**, 24187-24196.
52. K. Zeng and D. K. Zhang, *Prog Energ Combust*, 2010, **36**, 307-326.
53. J. A. Turner, *Science*, 2004, **305**, 972-974.
54. S. Gao, G. D. Li, Y. P. Liu, H. Chen, L. L. Feng, Y. Wang, M. Yang, D. J. Wang, S. Wang and X. X. Zou, *Nanoscale*, 2015, **7**, 2306-2316.
55. Y. Y. Ma, C. X. Wu, X. J. Feng, H. Q. Tan, L. K. Yan, Y. Liu, Z. H. Kang, E. B. Wang and Y. G. Li, *Energ Environ Sci*, 2017, **10**, 788-798.
56. J. Miao, F. X. Xiao, H. B. Yang, S. Y. Khoo, J. Chen, Z. Fan, Y. Y. Hsu, H. M. Chen, H. Zhang and B. Liu, *Sci Adv*, 2015, **1**, e1500259.
57. F. W. Fink, G. A. Dibari, E. L. White, W. K. Boyd and F. H. Haynie, *Mater Prot Perform*, 1971, **10**, 17-&.
58. S. H. Hsu, J. Miao, L. Zhang, J. Gao, H. Wang, H. Tao, S. F. Hung, A. Vasileff, S. Z. Qiao and B. Liu, *Advanced Materials* 2018, **1707261**
59. W. J. Luo, J. Hu, H. L. Diao, B. Schwarz, C. Streb and Y. F. Song, *Angew Chem Int Edit*, 2017, **56**, 4941-4944.
60. J. Wang, H. X. Zhong, Y. L. Qin and X. B. Zhang, *Angew Chem Int Edit*, 2013, **52**, 5248-5253.
61. K. Hedenstedt, N. Simic, M. Wildlock and E. Ahlberg, *J Electroanal Chem*, 2016, **783**, 1-7.
62. Y. F. Cheng and L. Niu, *Electrochem Commun*, 2007, **9**, 558-562.
63. L. Birry and A. Lasia, *J Appl Electrochem*, 2004, **34**, 735-749.

64. J. M. Jaksic, M. V. Vojnovic and N. V. Krstajic, *Electrochim Acta*, 2000, **45**, 4151-4158.
65. M. K. Bates, Q. Y. Jia, N. Ramaswamy, R. J. Allen and S. Mukerjee, *J Phys Chem C*, 2015, **119**, 5467-5477.
66. R. Subbaraman, D. Tripkovic, D. Strmcnik, K. C. Chang, M. Uchimura, A. P. Paulikas, V. Stamenkovic and N. M. Markovic, *Science*, 2011, **334**, 1256-1260.
67. Y. Tan, H. Wang, P. Liu, Y. Shen, C. Cheng, A. Hirata, T. Fujita, Z. Tang and M. Chen, *Energ Environ Sci*, 2016, **9**, 2257-2261.
68. D.-Y. Wang, M. Gong, H.-L. Chou, C.-J. Pan, H.-A. Chen, Yingpeng Wu, M.-C. Lin, M. Guan, J. Yang, C.-W. Chen, Y.-L. Wang, B.-J. Hwang, C.-C. Chen and H. Dai, *J Am Chem Soc*, 2015, **137**, 1587-1592.
69. Y. Zhang, Y. W. Liu, M. Ma, X. Ren, Z. Liu, G. Du, A. M. Asiri and X. P. Sun, *Chem Commun*, 2017, **53**, 11048-11051.
70. M. Gong, W. Zhou, M. J. Kenney, R. Kapusta, S. Cowley, Y. P. Wu, B. A. Lu, M. C. Lin, D. Y. Wang, J. Yang, B. J. Hwang and H. J. Dai, *Angew Chem Int Edit*, 2015, **54**, 11989-11993.
71. M. Gong, W. Zhou, M. J. Kenney, R. Kapusta, S. Cowley, Y. Wu, B. Lu, M. C. Lin, D. Y. Wang, J. Yang, B. J. Hwang and H. Dai, *Angew Chem Int Edit*, 2015, **54**, 11989-11993.

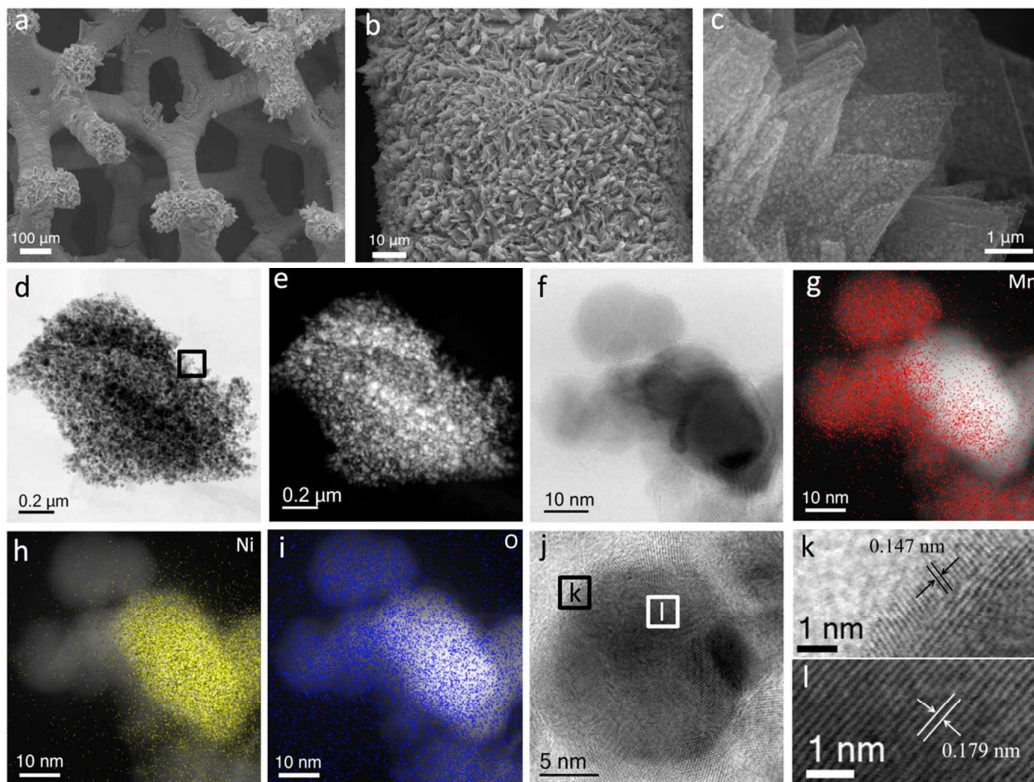


Figure 1. Microscographs of the as-prepared MnO-NiO-Ni/Ni-F. (a-c) SEM images of the MnO-NiO-Ni/Ni-F electrode under different magnifications. (d) STEM image of the MnO-NiO-Ni composites that have been scratched off from the electrode. (e) The corresponding HAADF image of (d). (f) High magnification STEM image of the MnO-NiO-Ni composites. (g-i) The corresponding elemental mappings of the MnO-NiO-Ni composites. (j) STEM of an individual NiO-Ni heterostructure within the MnO-NiO-Ni composite. (k) and (l) Enlarged STEM images of the areas marked in Figure 1j.

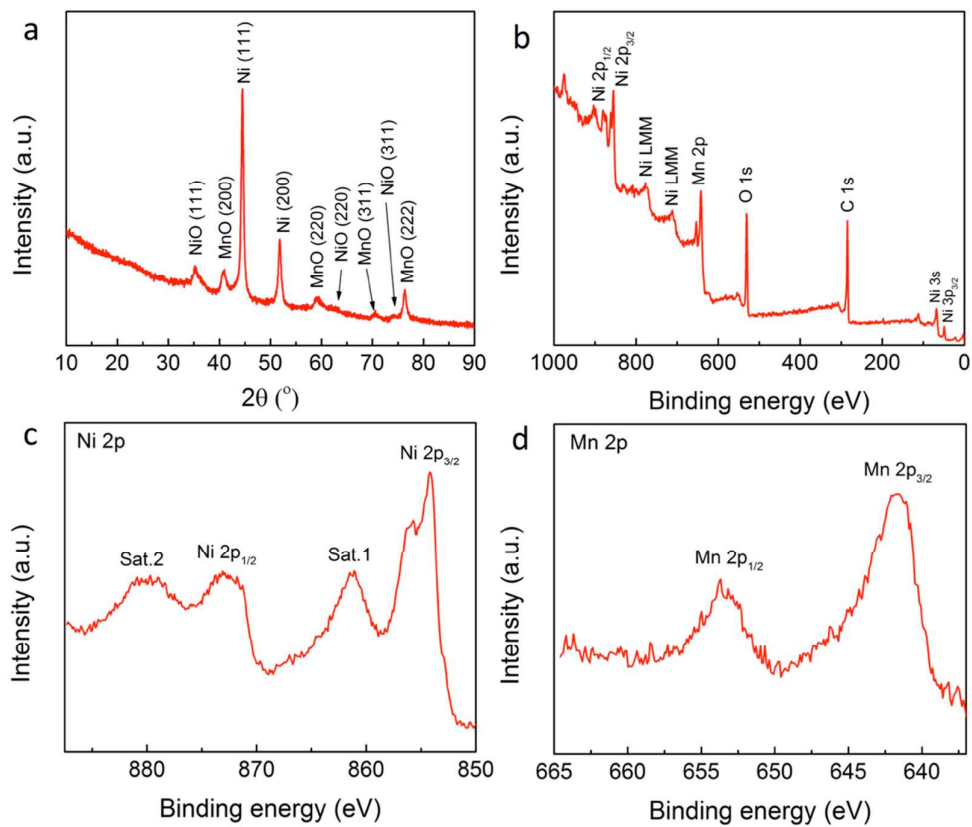


Figure 2. Spectroscopic measurements of the electrode prepared. (a) XRD pattern of the composite powders that are scratched off from the MnO-NiO-Ni/Ni-F electrode. **(b)** XPS survey spectrum of the MnO-NiO-Ni/Ni-F electrode. **(c-d)** High resolution Ni 2p and Mn 2p XPS spectra of the MnO-NiO-Ni/Ni-F electrode.

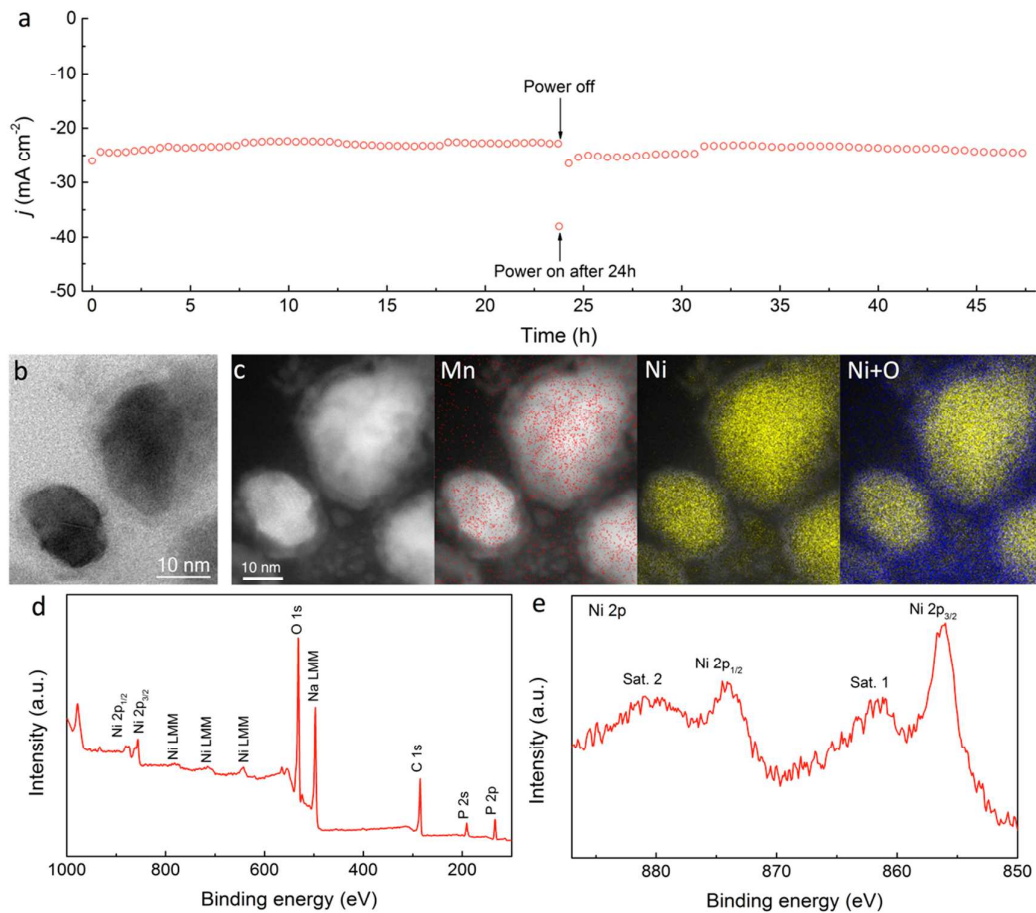


Figure 3. Electrochemical, physical and chemical characterizations of the MnO-NiO-Ni/Ni-F electrode in 1 M PBS for HER. (a) Chronoamperometric curve obtained with the MnO-NiO-Ni/Ni-F electrode in 1 M PB solution with a constant applied potential of -0.17 V. (b) STEM image of the composite material scratched off from the MnO-NiO-Ni/Ni-F electrode after 100 h of HER at an applied potential of -0.17 V and (c) its corresponding elemental mappings. (d) XPS survey spectrum and (e) high resolution XPS Ni 2p spectrum of the MnO-NiO-Ni/Ni-F electrode after 100 h of HER at an applied potential of -0.17 V.

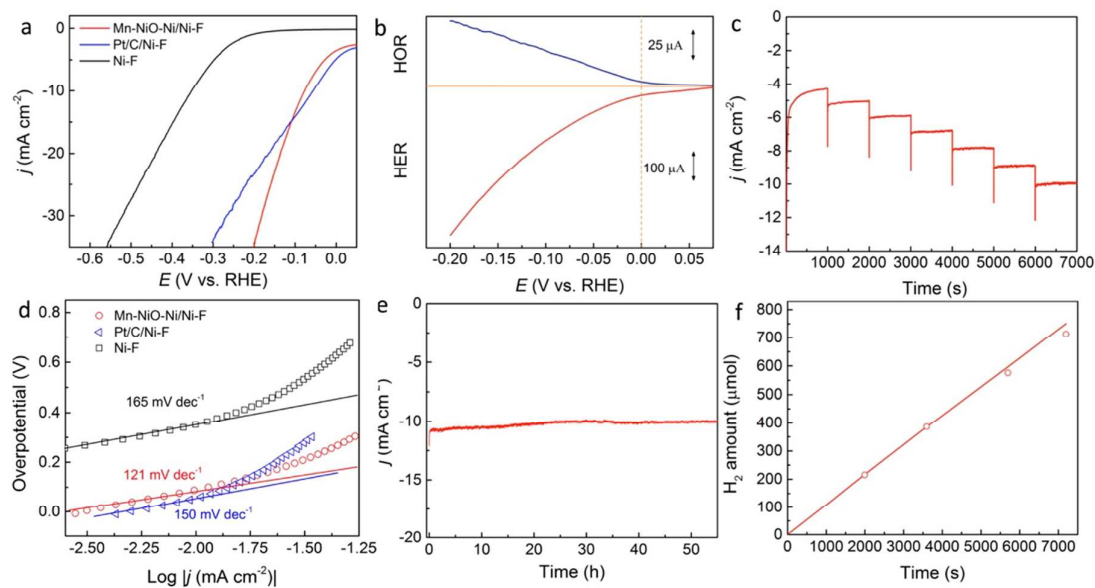


Figure 4. The HER catalytic performances of Mn-NiO-Ni/Ni-F in 1 M PB solution (pH = 7). (a) HER polarization curves obtained with the Mn-NiO-Ni/Ni-F, Pt/C/Ni-F, and bare Ni-F electrodes in 1 M PB solution at 1 mV s^{-1} . (b) Detection of H₂ evolution from the drop-casted Mn-NiO-Ni composite ink using rotating ring disk electrode measurements. The H₂ generated during the cathodic polarization scan is oxidized at the Pt ring at a constant potential of 0.33 V. (c) Multi-potential chronoamperometric curves obtained with the Mn-NiO-Ni/Ni-F electrode in 1 M PB solution. The potential started at -0.02 V and finished at -0.08 V, with a decrement of 10 mV every 1000 s. (d) Tafel plots of Mn-NiO-Ni/Ni-F, Pt/C/Ni-F, and bare Ni-F electrodes, respectively, derived from Figure 4a. (e) Chronoamperometric curve obtained with the Mn-NiO-Ni/Ni-F electrode in 1 M PB solution with a constant applied potential of -0.08 V. All current densities were obtained based on geometric surface area. (f) H₂ quantity (red dots) detected by a gas chromatography during HER in 1 M PB solution. The theoretical amount of hydrogen (red line) was calculated based on the total charge consumed during the same reaction period.

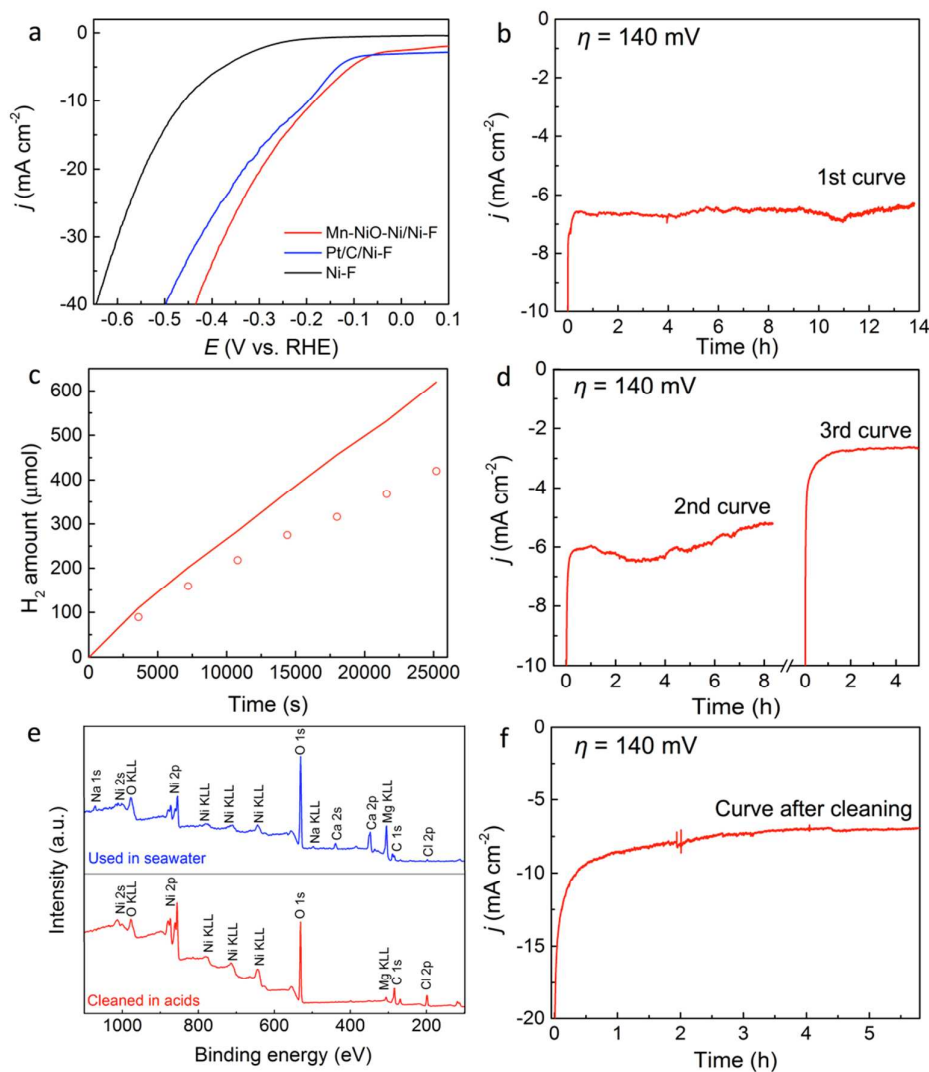


Figure 5. The HER catalytic performances of Mn-NiO-Ni/Ni-F in natural seawater. (a) HER polarization curves obtained with the Mn-NiO-Ni/Ni-F, Pt/C/Ni-F, and pristine Ni-F electrodes in seawater at 1 mV s⁻¹. (b) First chronoamperometric curve obtained with the Mn-NiO-Ni/Ni-F electrode in seawater at an applied potential of -0.14 V. (c) H₂ quantity (red dots) detected by a gas chromatography during HER in seawater. The theoretical amount of hydrogen produced (red line) was calculated by the charge consumed during the reaction assuming a 100% electricity-to-hydrogen conversion. (d) Second and third chronoamperometric curves obtained with the Mn-NiO-Ni/Ni-F electrode in seawater at the constant applied potential of -0.14 V. The interval between every measurement is 24 h. (e) XPS survey spectra of Mn-NiO-Ni/Ni-F after usage in seawater (blue line) and cleaned in diluted acidic solutions (red line). (f) The chronoamperometric curve obtained with the acid-cleaned Mn-NiO-Ni/Ni-F electrode in seawater at an applied potential of -0.14 V. All current densities were obtained based on geometric surface area.

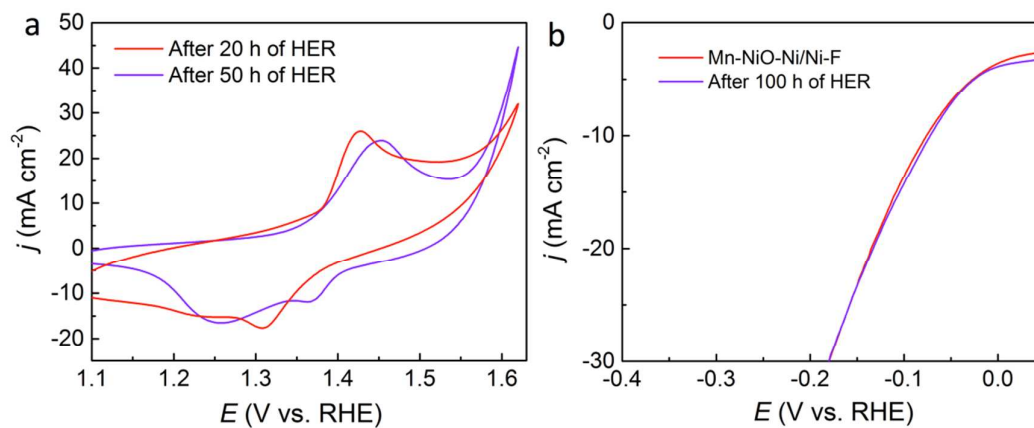


Figure 6. (a) CV obtained with Mn-NiO-Ni/Ni-F electrodes after 20 and 50 h of HER in 1 M PB solution at a constant applied potential of -0.17 V. The CV measurements were carried out in 1 M KOH solution at a scan rate of 5 mV s^{-1} . (b) HER polarization curves obtained with the Mn-NiO-Ni/Ni-F and Mn-NiO-Ni/Ni-F after 100 h of HER in 1 M PB solution at a constant applied potential of -0.17 V. The polarizations curves were measured in 1 M PB solution at 1 mV s^{-1} .

A sea-change: Manganese doped nickel/nickel oxide electrocatalysts for hydrogen generation from seawater

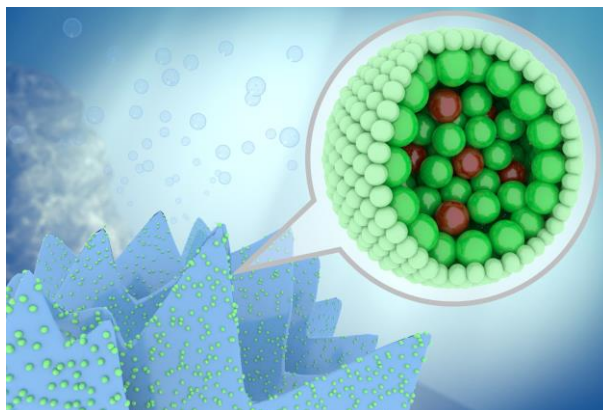
Xunyu Lu,* Jian Pan, Emma Lovell, Tze Hao Tan, Yun Hau Ng and Rose Amal*

Particles and Catalysis Research Group, School of Chemical Engineering, The University of New South Wales, Sydney, NSW 2052, Australia

Email: r.amal@unsw.edu.au

xunyu.lu@unsw.edu.au

Graphical Abstract



The facile and scalable synthesis of manganese-doped nickel/nickel oxide heterostructures with high activity, outperforming the Pt benchmark, in neutral electrolytes.